High-Temperature Large Strain Viscoelastic Behavior of Polypropylene Modeled Using an Inhomogeneously Strained Network

J. SWEENEY,[1] T. L. D. COLLINS,[1] P. D. COATES,[1] R. A. DUCKETT[2]

[1] Department of Mechanical and Medical Engineering/IRC in Polymer Science and Technology, University of Bradford, Bradford BD7 1DP, UK

[2] IRC in Polymer Science and Technology, University of Leeds, Leeds LS2 9JT, UK

Received 6 May 1998; accepted 23 August 1998

ABSTRACT: The effects of microstructural rearrangements during the stretching of semicrystalline polymers and the resultant inhomogeneous strains are modeled by rigid spheres embedded in a polymer network. This results in strain concentrations in the network, which is then caused to yield at realistic overall strains. To simulate the collapse of the original spherulitic morphology, the radii of the spheres decrease at a rate dependent on the shear stress imposed on them by the surrounding network. This results in time-dependent behavior. The resultant large strain viscoelastic model is implemented in a commercial finite element code and used to predict shapes of necking polypropylene sheet specimens at 150°C. Rate dependence of stress and stress relaxation are also predicted, and the model is shown to be generally effective in its predictions of shapes and forces up to large deformations. © 1999 John Wiley & Sons, Inc. J Appl Polym Sci 72: 563–575, 1999

Key words: constitutive equation; large deformation; polypropylene; finite element; necking

INTRODUCTION

In many key industrial processes, polypropylene is deformed to large strains at high temperatures below the melting point. The mathematical modeling of such processes requires that the constitutive behavior of the material be understood in a form suitable for tractable numerical schemes. To this end, we present a new model of polymer deformation and apply it to a semicrystalline polymer at high temperature. It is a development of earlier work[1,2] in which an elastic polymer network theory was shown to give useful predictions of the large deformation and necking of polypropylene at 150°C. This elastic model was generalized to include strain rate dependence[3] and thus to produce a more realistic representation of the shapes of necking polymer sheets. The present model uses the same underlying theory of the polymer network—that of Ball and colleagues[4]—but is nonlinear viscoelastic and can model both deformation and forces accurately up to large strains.

The principal attraction of the Ball and colleagues network from a modeling point of view is that it exhibits as inherent features the necking and strain hardening behavior characteristic of many polymers, while retaining the simplicity of an elastic theory. The developments referred to herein[1,2] were the result of modifications to it to

Correspondence to: J. Sweeney (j.sweeney@bradford.ac.uk).

Journal of Applied Polymer Science, Vol. 72, 563–575 (1999)
 CCC 0021-8995/99/040563-13

produce a theory that was quantitatively closer to observed stress–strain behavior. In its original form, the Ball and colleagues model predicts that the onset of necking for a uniaxially stretched material is at an extension ratio of 1.8 or higher, whereas the necking observed with polypropylene occurred in the range of 1.2–1.4. The purpose of the modification was to produce a theory valid for all strains and that removed the difficulty of the incorrect prediction of the necking strain. The present work is similarly motivated, but the nature of the adaptation that we introduce herein is such as to reflect the inhomogeneous nature of the material. The inhomogeneity of both structure and deformation of semicrystalline polymers has long been well known.[5] While not modeling the deformation mechanisms in detail, we take account of inhomogeneity in a simple way and derive a constitutive law that can be applied practically. The model that we produce has the further advantage that the viscoelastic nature of the material is included in a natural manner.

The new constitutive law is implemented within a finite element package. This makes it possible to assess its predictions of inhomogeneous deformations of stretching polymer specimens and the associated drawing forces. Comparison is made with laboratory experiments in which strains are measured using an image analysis technique. The validity of the predictions is found to be good, improving significantly on previous models.

MICROSTRUCTURAL BEHAVIOR

Most studies of the microstructure of deforming semicrystalline polymers have been conducted at room temperature, often using thin films of material. Peterlin[5] has described how, in uniaxial tension, the initially spherulitic structure of polyethylene or polypropylene is transformed into a microfibrillar structure. The transition takes place discontinuously, with "micronecking"—the formation of local high strain regions involving the breakdown of crystalline lamellae—the process by which the transformation is effected. Thus, for a necked tensile specimen, the spherulitic structure persists in the unnecked region, the material that has passed through the neck is fibrillar, and there are micronecks in the neck itself. It now seems that this particular micronecking phenomenon is not general, but a characteristic of uniaxial tension only,[6] and even then not at high temperature; the accompanying cavitation is not observed in polypropylene when the temperature is raised to 70°C.[7] Inhomogeneous deformation without cavitation is observed in other deformation modes, as demonstrated for high-density polyethylene in uniaxial compression[8] and in plane strain compression[9] and for polypropylene in shear.[7]

The general picture is that of inhomogeneous strain with local strains much higher than the overall macroscopic strain, as quantified by Plummer and Kausch,[10] who observed a mean local value of extension ratio of ~ 4 in a thin film of polypropylene stretched in tension to an overall ratio of 1.4. As deformation proceeds, there is evidence of fragmentation of crystallites and, as a consequence, chains from the lamellae being taken into the amorphous fraction.[11,12] Our proposed model is designed to capture the broad aspects of this behavior. It consists of a rigid phase embedded in a molecular network; this produces the effect of high local strains in comparison with the overall strain. A representative cube of material is assumed to contain some rigid phase in the form of a sphere at its center, with the cube volume excluded by the sphere occupied by the molecular network. The collapse of the initial structure is modeled by allowing the sphere to shrink at a rate dependent on the shear stress applied to it by the surrounding network. This has the effect of introducing nonlinear viscoelasticity into the model.

The rigid sphere may not be identified with a specific morphological feature, but rather is representative of the combined effect of a distribution of features. There are few direct morphological observations for the high temperature regime of this study to draw upon, but that of Olley and Bassett[13] on polypropylene at 150°C shows that inhomogeneous deformation remains an important phenomenon, and it seems likely that other broad features of the behavior at lower temperatures will still be relevant. Thus, the strain in highly deformed zones reaches an essentially constant value corresponding to a natural draw ratio, while the overall strain is still increasing[14] and, therefore, the sizes of undeformed zones must decrease.

THEORETICAL DEVELOPMENT

Network

The theory makes use of the model of Ball and colleagues,[4] which is hyperelastic and defined by the change in strain energy per unit volume, W, in response to principal extension ratios λ_1, λ_2, and λ_3:

$$\frac{W}{kT} = \frac{1}{2} N_c \sum_{i=1}^{3} \lambda_i^2 + \frac{1}{2} N_s \times \sum_{i=1}^{3} \left(\frac{(1+\eta)\lambda_i^2}{1+\eta\lambda_i^2} + \ln(1+\eta\lambda_i^2) \right) \quad (1)$$

k is the Boltzmann constant, T is the absolute temperature, N_c and N_s are, respectively, the number per unit volume of crosslinks and sliplinks, and η is a parameter governing the slipperiness of the sliplinks. η is nonnegative; for $\eta = 0$, we obtain the Gaussian chain model. For convenience, we rewrite (1) as

$$W = \frac{1}{2} N_c^* \sum_{i=1}^{3} \lambda_i^2 + N_s^* \sum_{i=1}^{3} b(\lambda_i) \quad (2)$$

where the parameters $N_c^* = kTN_c$ and $N_s^* = kTN_s$ have dimensions of stress. The incompressibility condition $\lambda_1\lambda_2\lambda_3 = 1$ is assumed to apply, and the constitutive equation is obtained by differentiating the strain energy

$$\sigma_{ii} = \lambda_i \frac{\partial W}{\partial \lambda_i} - p \quad (3)$$

to give the true principal stresses σ_{ii} ($i = 1, 2, 3$). p is a hydrostatic pressure arising from the assumption of incompressibility. For plane stress in the 1–3 plane, p can be eliminated and the use of eq. (2) gives

$$\sigma_{ii} = N_c^*(\lambda_i^2 - \lambda_2^2) + N_s^*[b'(\lambda_i) - b'(\lambda_2)] \quad (i = 1, 3) \quad (4)$$

where the primes denote differentiation.

Effective Strain

In the theory developed herein, the formulation of the Ball and colleagues model is retained, but the principal stretches λ_1, λ_2, and λ_3 are replaced by *effective* principal stretches $\bar{\lambda}_1$, $\bar{\lambda}_2$, and $\bar{\lambda}_3$. We are motivated by the fact that the polymer is inhomogeneous, consisting of hard, predominantly crystalline regions and relatively soft amorphous regions. We model a representative volume of material with a continuous Ball and colleagues model network in which a rigid sphere has been embedded. When such a medium is stretched, the strain in the network in the direction of stretch is greater than the macroscopic strain. This is a desirable feature for the modeling of necking polymer deformation, because, as noted previously,[1,2] the Ball and colleagues' model predicts that the onset of necking is at a higher strain than is observed. We define the effective stretches as values of the network stretches, averaged over a volume of network defined by a cube centered on the rigid sphere.

It is possible to envisage a variety of ways of distributing the rigid phase within a network matrix. Any such distribution is subject to the constraint that a representative volume of it be initially isotropic. To conform with this constraint and for computational simplicity, we adopt as our representative volume a cube with a rigid sphere at its center. The faces of the cube are always normal to the directions of principal stretch. This emphasizes the fact that the sphere cannot be specifically identified with a particular real morphological feature, but rather represents the overall effect of a distribution of such features. If the cube were fixed in orientation in space, then the sphere could correspond to a single physical feature, but then the model material would contain a regular array of spheres and would be anisotropic; a line normal to the cube faces through the sphere centers would contain a greater proportion of rigid material than would a line passing through cube corners.

In Figure 1, we show one octant of the representative cubic volume, with Cartesian axes along the principal stretch directions and the material in its undeformed state. The unit octant shown contains a sphere of nondimensional radius R such that $R < 1$. Rather than solve rigorously the continuum problem posed by the rigid inclusion, we make a simplifying assumption to facilitate a purely geometrical analysis. This is to the effect that, in the network material outside the sphere, lines along a principal direction are extended along the principal direction, with no motion normal to it. Now, consider such a line parallel to the 1 axis in Figure 1, joining the point (X_1, X_2, X_3) on the sphere surface to the point (1, X_2, X_3) on plane P. After stretching of the octant by a macroscopic extension ratio λ_1, this line joins the

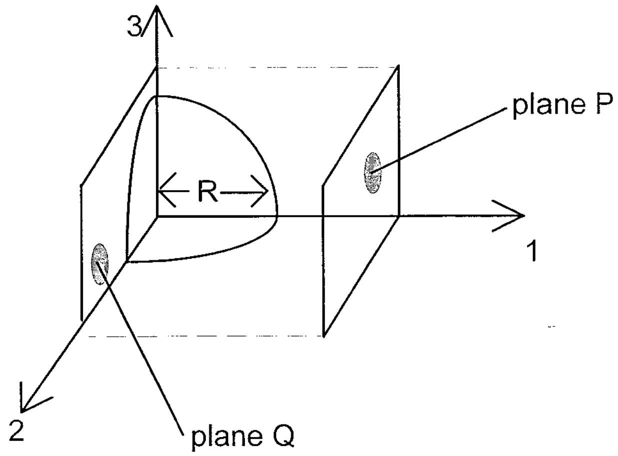

Figure 1 A unit octant containing network continuum intersecting a rigid sphere with center at its origin.

points (X_1, X_2, X_3) and (λ_1, X_2, X_3) and its extension ratio is

$$\lambda_1'(X_2, X_3) = \frac{\lambda_1 - X_1}{1 - X_1} \quad (5)$$

Lines that do not touch the sphere and join planes P and Q are at extension ratio λ_1. Averaging the extension ratios in the network contained in the unit octant between planes P and Q gives the effective extension ratio

$$\bar{\lambda}_1 = \int_0^R \int_0^{\sqrt{R^2 - X_2^3}} \lambda_1'(X_2, X_3)\, dX_2\, dX_3 + \lambda_1\left(1 - \tfrac{1}{4}\pi R^2\right) \quad (6)$$

Using relation (5) and the equation for the sphere surface in the integral gives

$$\bar{\lambda}_1 = \int_0^R \int_0^{\sqrt{R^2 - X_3^2}} \frac{\lambda_1 - \sqrt{R^2 - X_2^2 - X_3^2}}{1 - \sqrt{R^2 - X_2^2 - X_3^2}}\, dX_2\, dX_3 + \lambda_1\left(1 - \tfrac{1}{4}\pi R^2\right) \quad (7)$$

The same argument produces results for the other principal stretches, so that, in general

$$\bar{\lambda}_i = \int_0^R \int_0^{\sqrt{R^2 - X_k^2}} \frac{\lambda_i - \sqrt{R^2 - X_j^2 - X_k^2}}{1 - \sqrt{R^2 - X_j^2 - X_k^2}}\, dX_j\, dX_k + \lambda_i\left(1 - \tfrac{1}{4}\pi R^2\right) \quad \{i, j, k\} = \{1, 2, 3\} \quad (8)$$

The incompressibility condition applies for the effective stretches so that $\bar{\lambda}_1\bar{\lambda}_2\bar{\lambda}_3 = 1$.

The constitutive equations for plane stress are derived from the Ball and colleagues model expression of eq. (4), operating on the effective principal stretches:

$$\sigma_{ii} = N_c^*(\bar{\lambda}_i^2 - \bar{\lambda}_2^2) + N_s^*[b'(\bar{\lambda}_i) - b'(\bar{\lambda}_2)] \quad (i = 1, 3) \quad (9)$$

Sphere Radius

To produce realistic predictions, it is required that the sphere radius decrease as the deformation proceeds. It was found that a hyperelastic model, in which the sphere radius was a smooth function of the first strain invariant, could predict realistic stress–strain curves. However, such a model would be subject to the same limitations as previous elastic models,[1,2] in which the absence of any rate dependence of stress allows necks in the finite element model to form too abruptly and to be shaped such that the transition from unnecked to necked material occurs over too short a distance. It is therefore desirable to build rate dependence into the model. This can be done in a natural way, by retaining the hyperelastic network and defining a rate of decay of the sphere radius that is dependent on the stress. This reflects the physical expectation that structural rearrangement in the polymer will be the result of events driven by shear stress. As in the Tresca criterion, we assume the process to be driven by the maximum shear stress τ, which is calculated from the largest principal stress difference

$$\tau = \sigma_{\max} - \sigma_{\min} \quad (10)$$

where $\sigma_{\max}$ and $\sigma_{\min}$ are, respectively, the greatest and smallest principal stresses. It is assumed that the rate of change of sphere radius is defined by the expression

$$\frac{dR}{dt} = -(R - R_\infty)A[\exp(B\tau) - 1] \quad (11)$$

This is essentially an empirical expression that results in a model with realistic overall performance, provided that the parameters A, B, and R_∞ are assigned appropriate values. R_∞ is the lower limit to the sphere radius R; to complete the specification, R_0, the initial value of R for unstrained material, must be defined.

Finite Element Implementation

The theory was introduced into the finite element package ABAQUS as a user-defined material *via* the UMAT facility.[15] A two-dimensional formulation was implemented using the constitutive equations [eq. (9)]. The effective extension ratios must be calculated from the macroscopic extension ratios using eq. (8). The inner integral in these relations can be evaluated exactly, to give

$$\bar{\lambda}_i = \int_0^R (\lambda_i - 1)\left[\frac{\sin^{-1}(\sqrt{R^2 - X^2}) + \pi/2}{\sqrt{1 - R^2 + X^2}} - \frac{\pi}{2}\right] + \sqrt{R^2 - X^2}\, dX + \lambda_i\left(1 - \frac{1}{4}\,\pi R^2\right) \quad (i = 1, 2, 3) \qquad (12)$$

The single integrals in eq. (12) are evaluated using a quadrature method (NAG routine D01AHF). Equation (12) is used for the two in-plane principal directions, with the effective stretch in the third direction obtained using the incompressibility condition. The effective extension ratios so defined are used as input into the relations [eq. (9)] to give the principal stresses; from these, stresses in any required nonprincipal directions are obtained using the appropriate second-order transformation, about an angle to the principal direction supplied by a standard ABAQUS routine.

Also required is the Jacobian matrix J linking the stress and strain increments. This is defined for arbitrary in-plane directions x and z by

$$\begin{bmatrix} \Delta\sigma_{xx} \\ \Delta\sigma_{zz} \\ \Delta\sigma_{xz} \end{bmatrix} = \begin{bmatrix} \bar{J}_{11} & \bar{J}_{13} & \bar{J}_{15} \\ \bar{J}_{31} & \bar{J}_{33} & \bar{J}_{35} \\ \bar{J}_{51} & \bar{J}_{53} & \bar{J}_{55} \end{bmatrix} \begin{bmatrix} \Delta e_{xx} \\ \Delta e_{zz} \\ \Delta e_{xz} \end{bmatrix} \qquad (13)$$

where $\Delta\sigma_{xx}$, $\Delta\sigma_{zz}$, and $\Delta\sigma_{xz}$ are increments in true stress arising from increments in natural strain Δe_{xx}, Δe_{zz}, and Δe_{xz}. Components of J in principal directions are denoted by the lack of an overbar, and four of these (J_{11}, $J_{13} = J_{31}$ and J_{33}) are obtained *via* the expression

$$J_{ij} = \frac{\partial\sigma_{ii}}{\partial e_{jj}} = \frac{\partial\sigma_{ii}}{\partial\bar{\lambda}_j}\frac{d\bar{\lambda}_j}{d\lambda_j}\frac{d\lambda_j}{de_{jj}} \quad (i = 1, 3) \qquad (14)$$

where $\frac{\partial\sigma_{ii}}{\partial\bar{\lambda}_j}$ is obtained by differentiating eq. (9), $\frac{d\bar{\lambda}_j}{d\lambda_j}$ by differentiating eq. (12) to give

$$\frac{d\bar{\lambda}_j}{d\lambda_j} = \int_0^R \left[\frac{\sin^{-1}(\sqrt{R^2 - X^2}) + \pi/2}{\sqrt{1 - R^2 + X^2}} - \frac{\pi}{2}\right] dX + \left(1 - \frac{1}{4}\,\pi R^2\right) \qquad (15)$$

and $\frac{d\lambda_j}{de_{jj}} = \lambda_j$. The symbolic algebra package Maple is used to differentiate eq. (9) and give the result as blocks of FORTRAN, and the integral in eq. (15) is evaluated by quadrature (NAG routine D01AHF). In principal directions, $J_{15} = J_{35} = J_{51} = J_{53} = 0$.

To complete the definition of J in this axis set, we note that $J_{55} = \frac{1}{2}(J_{11} + J_{33}) - J_{13}$, a result obtained by considering shear behavior in a rotated axis set. The Jacobian matrix in arbitrary axes is obtained using the appropriate fourth-order transformation, with the rotation angle supplied by a standard ABAQUS subroutine. The result is asymmetric.

The analysis is incremental; in each increment, the value of sphere radius R is updated using eq. (11), with the value of shear stress τ stored from

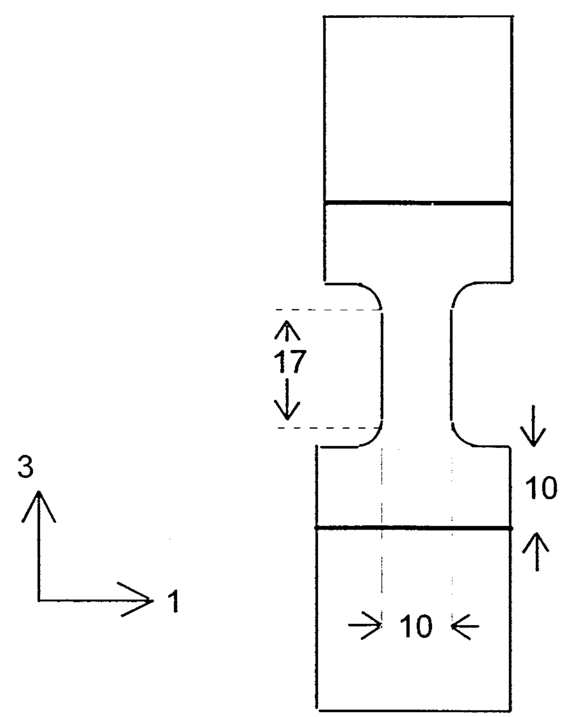

Figure 2 Uniaxial tensile specimen. Bold horizontal lines represent the extent of the gripped area. Dimensions are in millimeters, and specimen thickness is 1.6 mm.

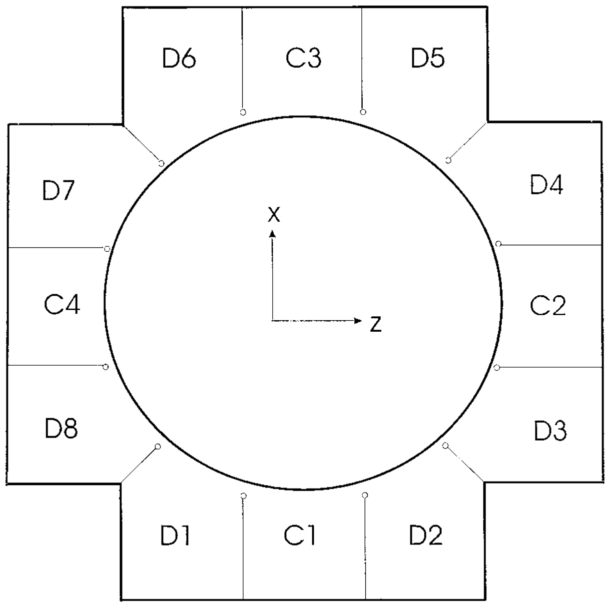

Figure 3 Constant width tensile specimen. Inner circular area of 130 mm diameter is of 0.8 mm thickness, compared with the 1.6 mm thickness of the rest of the sheet. Gripping is at tabs C1–C4, D1–D8. Drawing is along the z direction, with tabs C1, C3, D1, D2, D5, and D6 restrained from lateral motion. Necks initiate between these grips as they separate.

the previous increment. The size of the time steps is controlled so as not to degrade the accuracy of the analysis.

EXPERIMENTAL

Tensile stretching experiments have been conducted on polypropylene at 150°C. The material, the same as used previously,[1–3] was obtained in commercial sheet form. It was manufactured by Tiszai Vegyi Kombinat, Hungary, and designated as grade K-899. Molecular weights as obtained by gel permeation chromatography were $\bar{M}_w = 452{,}600$ and $\bar{M}_n = 95{,}760$.

Uniaxial experiments on specimens of the geometry illustrated in Figure 2 were performed using an Instron testing machine operating at constant crosshead speeds, with the specimen in a temperature-controlled oven. In these experiments, the specimens, which deform inhomogeneously, were viewed through the glass oven door using a CCD camera, and the strains deduced by the analysis of digitized images, by a method reported previously.[16] Tests were run at constant speeds that were varied between 0.1 and 0.4 mm s^{-1}, corresponding to initial shear strain rates of 4.1×10^{-3} and 1.65×10^{-2} s^{-1} and maximum

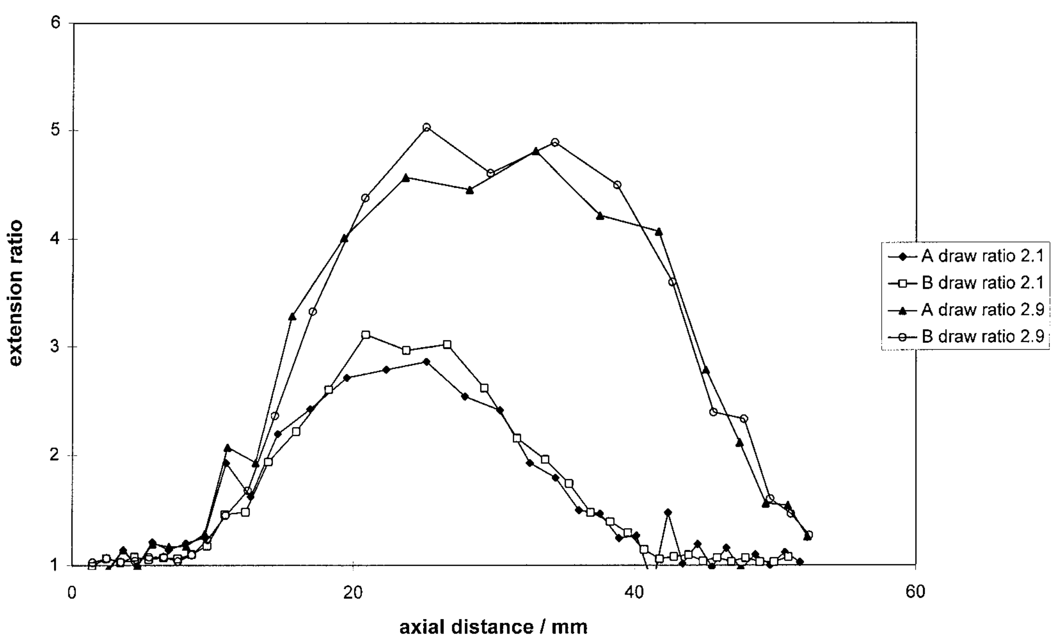

Figure 4 Comparison of strain fields obtained by image analysis of two nominally identical experiments A and B. Tensile specimens of the type depicted in Figure 2 are drawn at 0.2 mm s^{-1}. Profiles of extension ratio in the gauge length are shown at overall draw ratios of 2.1 and 2.9.

Table I Model Parameters

N_c^* (MPa)	N_s^* (MPa)	η	A (s^{-1})	B (MPa)	R_0	R_∞
0.257	1.70	0.23	5×10^{-5}	1.49	0.99	0.6

extensions corresponded to overall stretching of the gauge lengths up to an extension ratio of 3. Stress relaxation experiments were also performed, with the specimens strained at 0.2 mm s^{-1} and then held at almost constant extension (an extension speed of 8.3×10^{-4} mm s^{-1}), whereas the force was monitored for up to 1000 s. The use of a nonzero secondary speed was entirely for experimental convenience. These experiments differ from the conventional stress relaxation experiment, in that strains are not constant throughout the specimen and continue to change with time after the initial strain has been applied.

As noted previously,[2] uniaxial extension experiments provide insufficient information to define uniquely the parameters characterizing a constitutive model of this level of complexity. A biaxial testing machine featuring a temperature-controlled oven was used to deform sheet specimens under conditions of planar extension, while measuring forces both along and across the stretch direction. The specimen geometry is shown in Figure 3. A circular gauge area is machined to approximately half the thickness of the original sheet, whereas the rest of the specimen retains the original thickness. This is to ensure that deformation is not confined to the outer sections where the specimen is gripped. Necking is initiated from the ends of the slits that separate the gripped boundary tabs as the experiment proceeds and the grips separate. These experiments were conducted at an accelerating testing speed, corresponding to a constant shear rate of 10^{-2} s^{-1}. The specimens were stretched to an overall axial extension ratio of 2.2, and both axial and lateral forces monitored. Deformation fields at the completion of the tests were measured by means of meshes drawn onto the specimen surfaces. Experimental data from these experiments have also been reported elsewhere.[2]

RESULTS AND MODELING

Uniaxial Stress–Strain Tests

Both the deformation fields as measured using the image analysis technique and the associated drawing forces are compared with the model predictions. First, we demonstrate the reproducibility of the measured deformations by comparing two experiments conducted under the same conditions. In Figure 4, the profiles of axial extension ratio are compared for testing speeds of 0.2 mm s^{-1}. The images correspond to overall stretch ratios of 2.1 and 2.9. This shows the level of reproducibility that is typically achieved. It justifies the use of data from only one image to assess the quality of the model predictions as discussed herein.

The theory of the Theoretical Development section has been implemented in the finite element package ABAQUS as described. Values of the seven material parameters were chosen largely on a trial-and-error basis to match the various experimental observations, which were: shapes of deformed specimens, stress–strain curves, rate

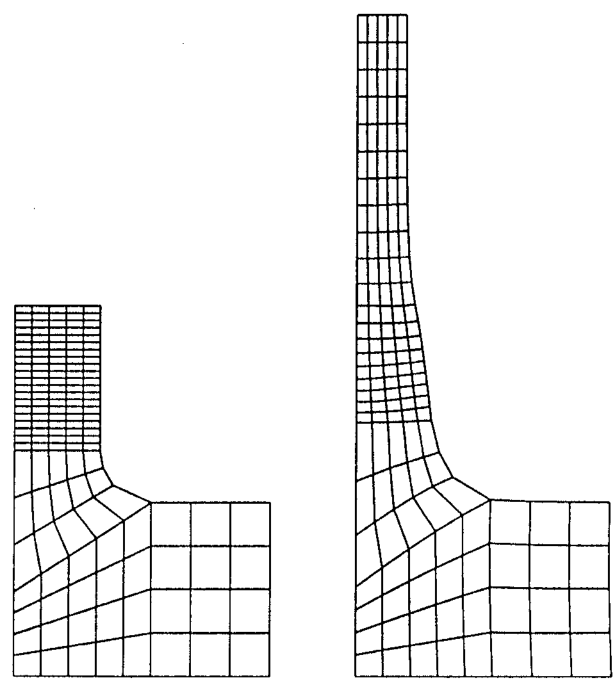

Figure 5 Quarter finite element model of the stretching of the tensile specimen of Figure 2, with upper horizontal and left hand vertical boundaries axes of symmetry. On the right, the deformed specimen is shown extended to an overall draw ratio of 3.0.

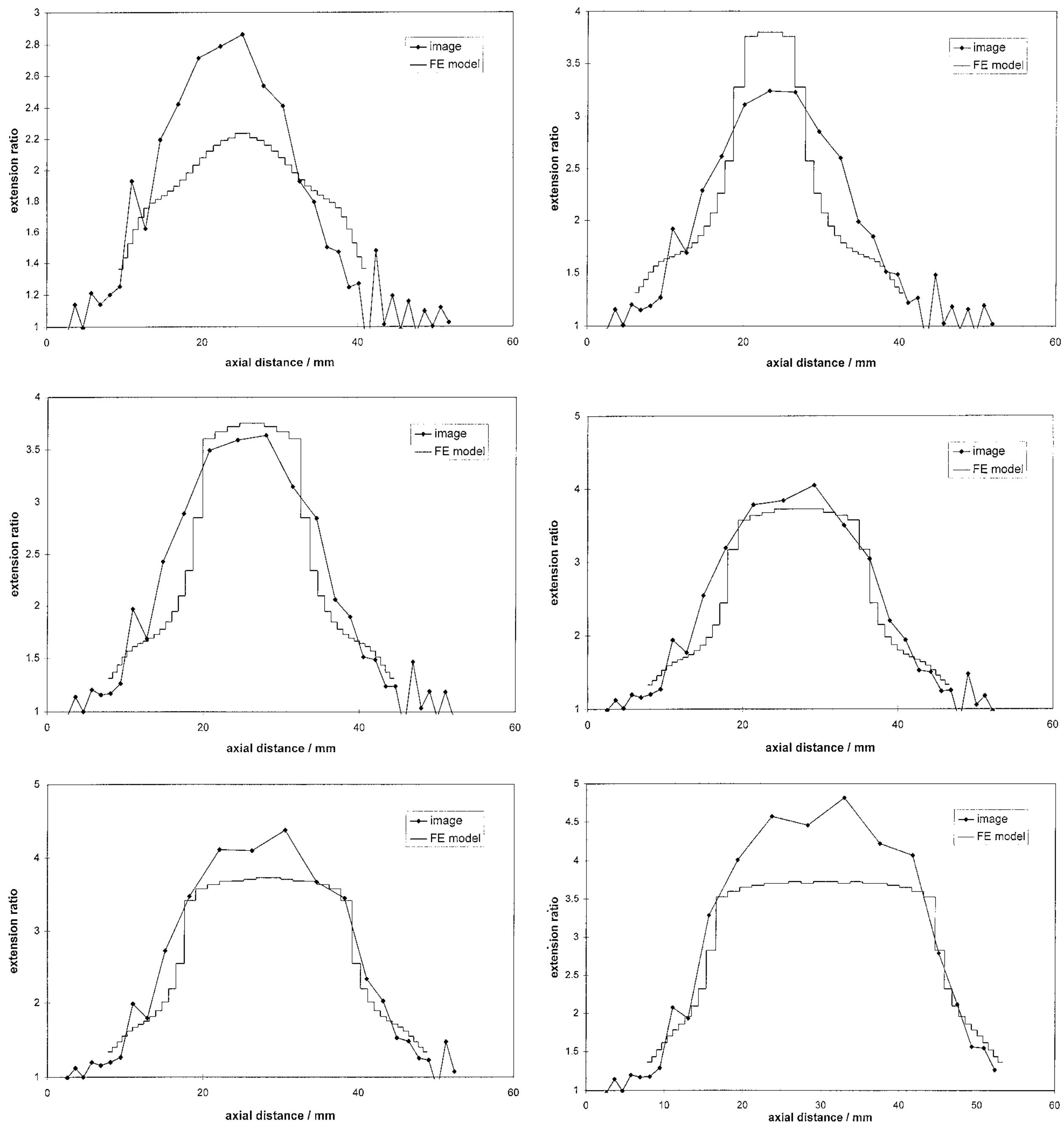

Figure 6 Comparisons of observed and modeled profiles of extension ratio for the tensile specimen of Figure 2 and model of Figure 5. Overall draw ratios are: (a) 2.1, (b) 2.2, (c) 2.3, (d) 2.5, (e) 2.6, and (f) 2.9. FE, finite element.

dependence of peak stresses, and stress relaxation in uniaxial extension. As well as the finite element implementation, the theory was also calculated for constant strain rates to assist in the search for an appropriate set of constants. The values used are given in Table I. They are not unique, in the sense that a somewhat different set of values can give very similar predictions. The value of η was fixed at 0.23, as recommended by Ball and colleagues.[4] As noted in the Introduction, it was expected that the rigid spheres would introduce local strain concentrations so that the network would reach its peak load at an overall extension ratio much lower than that of $\sim$ 1.8

naturally associated with the Ball and colleagues model. The overall extension ratio associated with the load peak was strongly influenced by the initial sphere radius R_0, and it was found necessary to assign a value approaching the maximum of $R_0 = 1$ to cause the load to peak at a realistically small strain. A value of exactly 1 is associated with an infinitely large local strain and cannot be used in eq. (12) for calculating effective strain.

In Figure 5, the finite element model representing a quarter of the tensile specimen of Figure 2 is shown. The deformed model is at the maximum overall extension ratio of 3. In Figure 6, the deformation of the model at progressive stages is shown, compared with observations using image analysis of experiment A of Figure 4. Overall, the agreement is good, although the initial development of strain in the model is too slow, as shown in Figure 6(a), which corresponds to an overall draw ratio of 2.1. In the model, the strain field is soon characterized by a natural draw ratio of $\sim$ 3.7, which stays essentially constant throughout the remainder of the deformation, from Figure 6(b) (overall draw ratio 2.2) to Figure 6(f) (overall draw ratio 2.9). The major difference between the experiments and the predictions is that, in the experiments, the natural draw ratio is a less well-defined quantity, with the maximum strain continuing to increase as the experiment progresses. In contrast, the model is characterized by classic stable necking. At this stage, the material near the center of the model neck is approaching an elastic state, because the sphere radius R is close to R_∞, and the surrounding network is itself elastic. In the range that has been investigated (defined by half and double the 0.2 mm s^{-1} of this experiment) testing speed has little influence on the deformation fields either experimentally or theoretically.

The observed and predicted nominal stress–strain results for experiment A are compared in Figure 7. In the experiments, the observed strain is the maximum axial strain, which occurs near the neck center and corresponds to a shear-free state. The corresponding model strain is on the vertical symmetry axis of Figure 5, derived from the deformed length of the side of the topmost element. The stress–strain curves are peculiar to this experimental regime, in the sense that they are the product of a complex strain rate history. The agreement is very good, with the only significant difference being that the model strain does not proceed beyond a natural draw ratio, an effect noted in the previous discussion of the deforma-

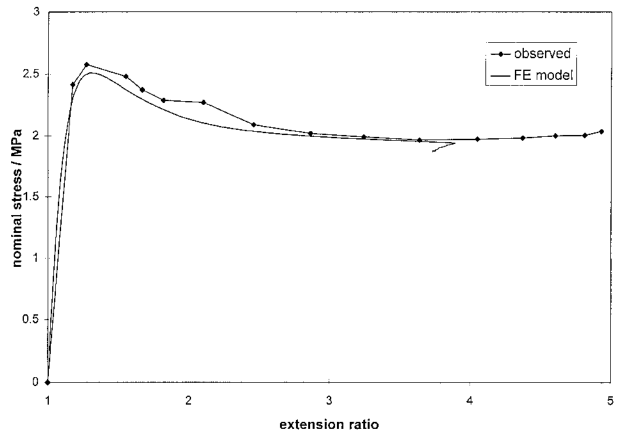

Figure 7 Observed and predicted nominal stress–strain curves for the tensile specimen. The model curve shows no strain hardening, because it corresponds to stable necking, with some decay in stress accompanying a degree of elastic recovery. FE, finite element.

tion fields. Note the excellent agreement between measured and modeled yield strains—this aspect has not been satisfactorily dealt with in previous formulations.

Only a limited range of strain rates has been explored in this study. To examine the validity of the predictions of stress as a function of strain rate, we compare the predictions of the model in constant strain rate uniaxial conditions with results from the stretching of thin sheets of the polypropylene material at this temperature reported previously.[1] The peak nominal stresses are plotted in Figure 8. The predicted rate dependence is consistent with the observations for the range considered, which corresponds to a ratio of 32 difference between the highest and lowest rate. As noted previously,[3] the strength of the rate dependence has a crucial effect on the predicted neck shape, so this degree of consistency is to be expected, given the validity of the shape predictions demonstrated in Figure 6.

Constant Width Tests

In Figure 9, we show the deformed and undeformed finite element models representing the constant width specimen of Figure 3. The theory of the Theoretical Development section, together with the parameter values of Table I, were again used in this analysis. Deformation fields are compared in Figure 10 in terms of extension ratio along the stretching (z) axis at the final state of deformation that corresponds to an overall exten-

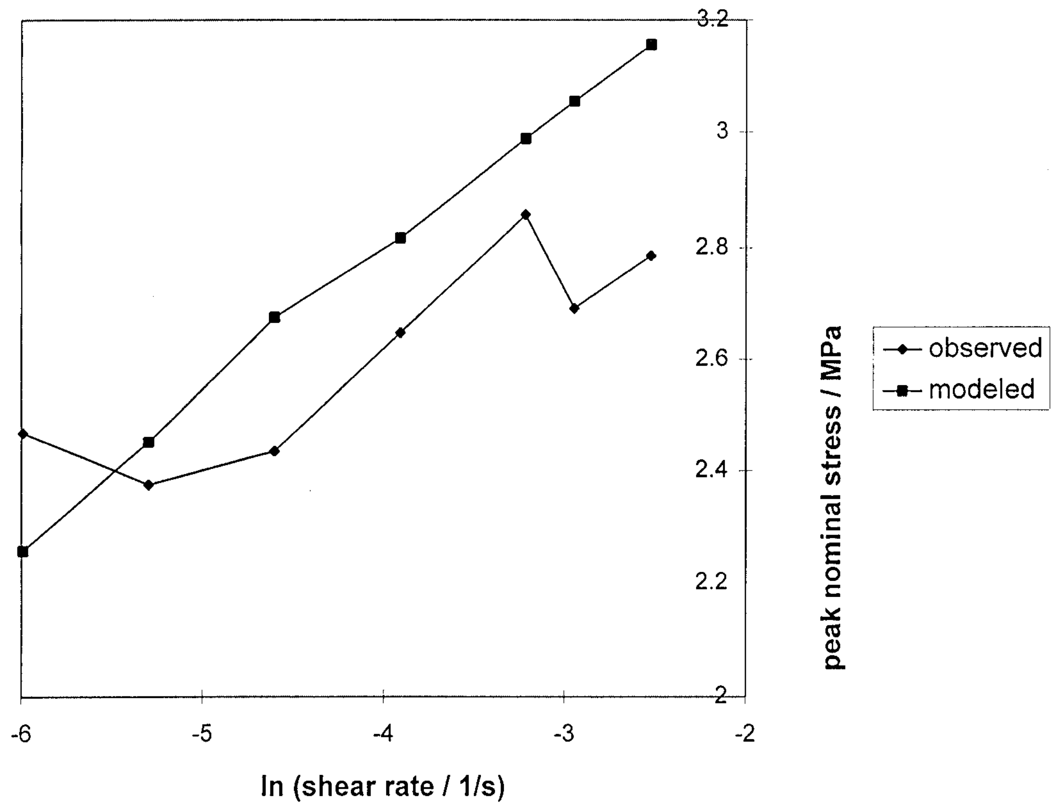

Figure 8 Observed and predicted rate dependences for the peak nominal stress in tensile stretching.

sion ratio of 2.2. A good agreement is shown. Predictions of the forces both along and normal to the stretch direction are shown in Figure 11, in terms of nominal stress, and agreement is good for the forces in both directions. As noted previously,[2] the lateral force in this kind of experiment strongly depends on the network parameter η, so that this level of agreement justifies the value of 0.23 that we have used.

Uniaxial Stress Relaxation Tests

The nature of the time dependence exhibited by the constitutive model influences both the rate dependence of stress and the predicted shapes, and so it has been subject to some degree of verification *via* the experiments reported so far. For a more direct evaluation, stress relaxation tests as described in the Experimental section have

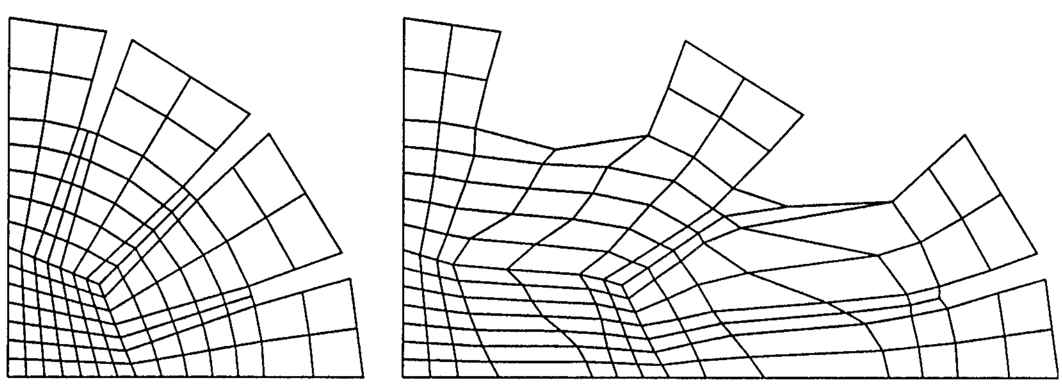

Figure 9 Quarter model of constant width specimen of Figure 3. On the right, the deformed model corresponds to an overall draw ratio of 2.2.

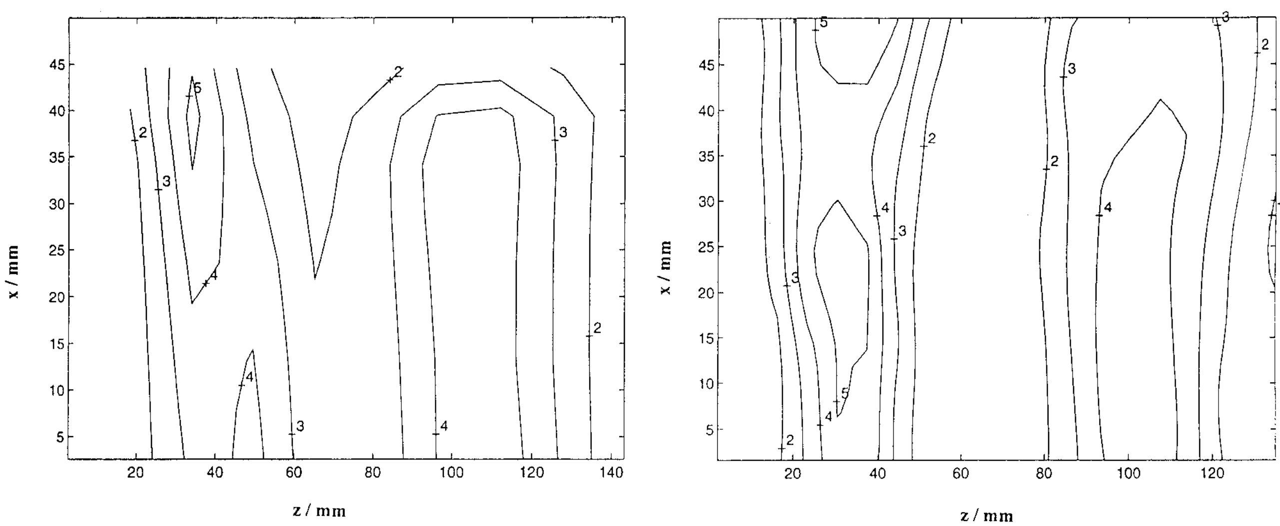

Figure 10 Comparison of observed (left) and modeled (right) axial (z-direction) extension ratios for the constant width specimen at the overall draw ratio of 2.2.

been performed and modeled using the theory of the Theoretical Development section and parameters of Table I.

Results for two levels of strain are presented, corresponding to overall extension ratios of 1.5 and 3.0 on the specimen of Figure 2. The same

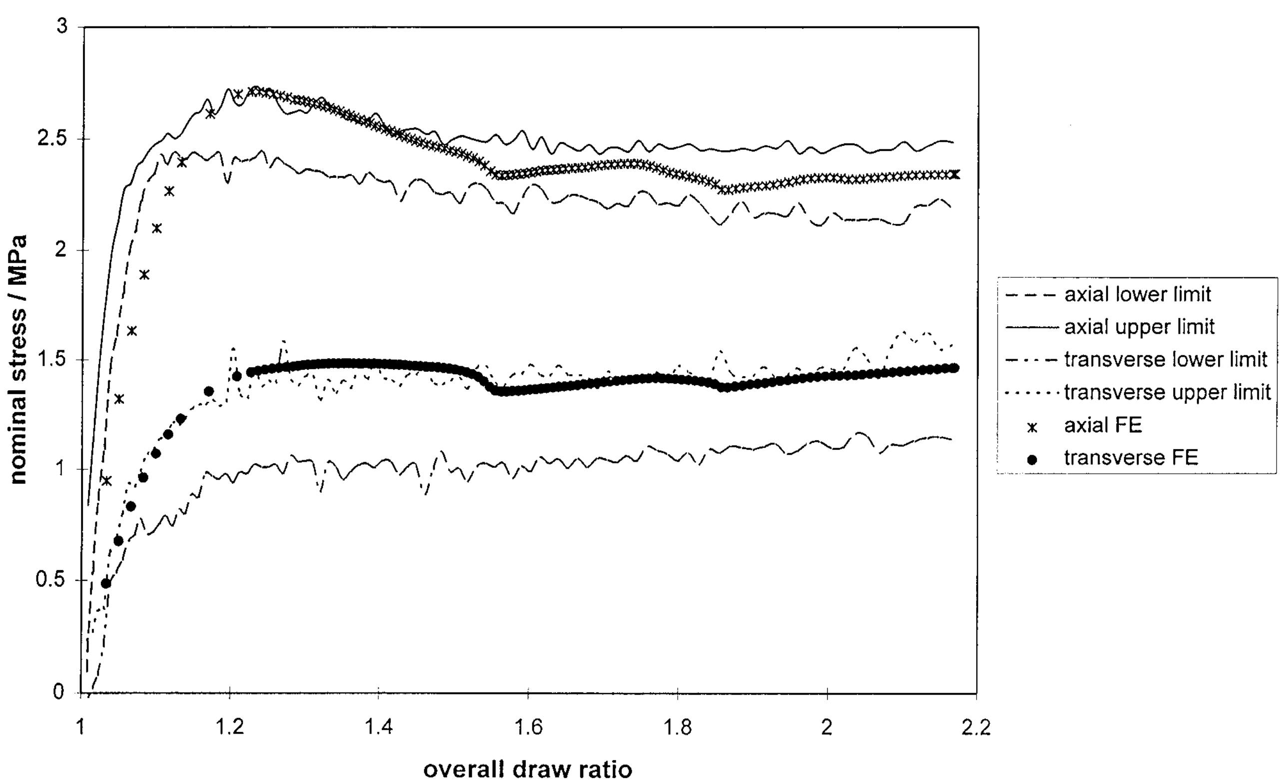

Figure 11 Comparison of observed and predicted nominal stresses for the constant width test. Both axial and transverse stresses are compared. Observed results are an average of five experiments, with the upper and lower limits spanning 90% confidence intervals. FE, finite element.

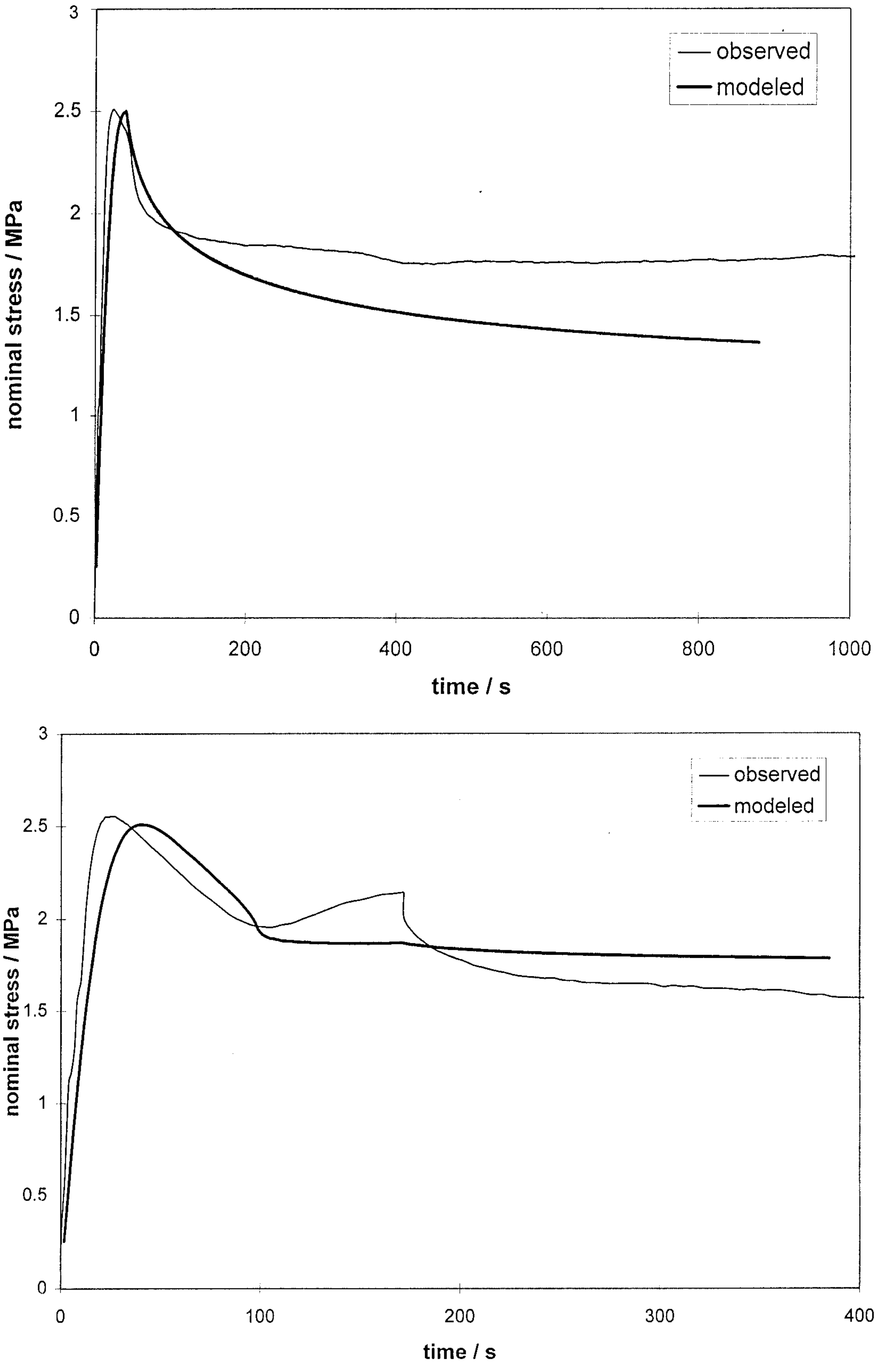

Figure 12 Stress relaxation of tensile specimen at an overall draw ratio of (a) 1.5 and (b) 3.0. The first maximum corresponds to yield, with the initial deformation being stopped at 40 s in (a) where an inflexion is apparent in the observed curve, and 170 s in (b) where stress drops are visible in both curves.

finite element model geometry as for the stress–strain tests, that of Figure 5, was used. Both the initial testing speed and the secondary slow speed, as described in the Experimental section, were used as model boundary conditions. The observed nominal stresses are compared with the predictions as a function of time in Figure 12. In Figure 12(a), for the lower strain, the model stress tends to a lower asymptotic value than that observed, whereas at the higher strain shown in Figure 12(b), the prediction is high. After the initial loading, the strain in the model neck is lower than in the experiment, having reached the natural draw ratio and the stable necking condition; there is thus no strain hardening in the model, whereas there is in the experiment. The model neck is in a near-elastic state at the end of the initial loading period and the stress in the model can then decrease only as a result of elastic recovery in the neck. The approach to the elastic state can therefore be seen to be a cause of both the low strain predictions in Figure 6(d,e) and of the lack of strain hardening in Figure 12(b). The stress relaxation experiment provides a relatively sensitive test of the constitutive model, particularly at the high strain when the strain in the model neck differs from that in the specimen neck.

DISCUSSION AND CONCLUSIONS

The proposed model gives useful predictions of stresses and strain fields for the high temperature stretching of polypropylene. The shapes of necking specimens, the associated drawing forces and their dependence on the deformation rate, and stress relaxation, are all represented to reasonable levels of accuracy.

The most important simplifying assumption is that the polymer network is elastic. All the time dependence is thus associated with the shrinking of the embedded spheres, so that when they reach their ultimate radius and cease to shrink, the model has an elastic response. This is the probable reason for some of the unrealistic aspects of the model. In the uniaxial stretching experiments, the model predicts classic stable necking, with very nearly constant strain in the neck as the deformation progresses [see Figure 6(b–f)]; this is a result of the material in the model neck having evolved to a nearly elastic state. In the real material, the necking is only approximately stable, and the strain in the neck continues to increase, as a consequence of the material's continuing to be viscoelastic. Similarly, at high strains, the stress in the model ceases to relax at too early a stage, compared with the experiments [see Figure 12(b)].

The obvious next step would be to include viscoelasticity into the network. This would entail a model with more parameters than the seven characterizing the present one. A strong positive aspect of the present model is that it has been successfully implemented in a commercial finite element package and converges readily. In this context, the constitutive equation presented herein performs more efficiently than the elastic model described previously.[2] This combination of general effectiveness and computational efficiency suggests a wider potential application to the deformation of semicrystalline polymers.

REFERENCES

1. Sweeney, J.; Ward, I. M. J Mech Phys Solids 1996, 44, 1033.
2. Sweeney, J.; Collins, T. L. D.; Coates, P. D.; Ward, I. M. Polymer 1997, 38, 5991.
3. Sweeney, J.; Collins, T. L. D.; Coates, P. D.; Unwin, A. P.; Ward, I. M. ASME J Eng Math Tech 1997, 119, 228.
4. Ball, R. C.; Doi, M.; Edwards, S. F.; Warner, M. Polymer 1981, 22, 1010.
5. Peterlin, A. J Mater Sci 1971, 6, 490.
6. Lin, L.; Argon, A. S. J Mater Sci 1994, 29, 294.
7. Aboulfaraj, M.; G'Sell, C.; Ulrich, B.; Dahoun, A. Polymer 1995, 36, 731.
8. Bartczak, Z.; Cohen, R. E.; Argon, A. S. Macromolecules 1992, 25, 4692.
9. Galeski, A.; Bartczak, Z.; Argon, A. S.; Cohen, R. E. Macromolecules 1992, 25, 5705.
10. Plummer, C. J. G.; Kausch, H.-H. Macromol Chem Phys 1996, 197, 2047.
11. G'Sell, C.; Dahoun, A. Mater Sci Eng 1994, A175, 183.
12. Way, J. L.; Atkinson, J. R. J Mater Sci 1971, 6, 102.
13. Olley, R. H.; Bassett, D. C. J Macromolec Sci-Phys 1994, B33, 209.
14. Tarin, P. M.; Thomas, E. L. Polym Eng Sci 1979, 19, 1017.
15. Hibbitt, Karlsson and Sprensen, Inc. ABAQUS, version 5.5; Hibbitt, Karlsson, and Sprensen, Inc.: Providence, RI, 1995.
16. Haynes, A. R.; Coates, P. D. J Mater Sci 1996, 31, 1843.